Journal of Geophysical Research: Atmospheres

RESEARCH ARTICLE
10.1029/2018JD028971

The Simulation of Stratospheric Water Vapor Over the Asian Summer Monsoon in CESM1(WACCM) Models

Xinyue Wang[1], Yutian Wu[2], Wen-wen Tung[1], Jadwiga H. Richter[3], Anne A. Glanville[3,4], Simone Tilmes[3,4], Clara Orbe[5], Yi Huang[6], Yan Xia[7], and Douglas E. Kinnison[4]

[1]Department of Earth, Atmospheric, and Planetary Sciences, Purdue University, West Lafayette, IN, USA, [2]Lamont-Doherty Earth Observatory, Columbia University, Palisades, NY, USA, [3]Climate and Global Dynamics Laboratory, National Center for Atmospheric Research, Boulder, CO, USA, [4]Atmospheric Chemistry, Observations and Modeling Laboratory, National Center for Atmospheric Research, Boulder, CO, USA, [5]NASA Goddard Institute for Space Studies, NY, USA, [6]Department of Atmospheric and Oceanic Sciences, McGill University, Montreal, Quebec, Canada, [7]Department of Atmospheric and Oceanic Sciences, Peking University, Beijing, China

Key Points:
- The discrepancies in simulating SWV over the Asian summer monsoon region are commonly found in WACCM experiments
- The UTLS temperature over the central Pacific Ocean is crucial in confining the SWV within the Asian summer monsoon anticyclone
- Model with high vertical resolution resolves the UTLS temperature more accurately which better confines the SWV within the transport barrier

Supporting Information:
- Supporting Information S1
- Figure S1
- Figure S2
- Figure S3
- Figure S4
- Figure S5
- Figure S6
- Figure S7

Correspondence to:
X. Wang,
wang2807@purdue.edu

Citation:
Wang, X., Wu, Y., Tung, W.-W., Richter, J. H., Glanville, A. A., Tilmes, S., et al. (2018). The simulation of stratospheric water vapor over the Asian summer monsoon region in CESM1(WACCM) models. *Journal of Geophysical Research: Atmospheres*, *123*. https://doi.org/10.1029/2018JD028971

Received 11 MAY 2018
Accepted 24 SEP 2018
Accepted article online 9 OCT 2018

©2018. American Geophysical Union. All Rights Reserved.

Abstract Previous observational studies have found a persistent maximum in stratospheric water vapor (SWV) in the upper troposphere lower stratosphere (UTLS) confined by the upper-level anticyclone over the Asian summer monsoon region. This study investigates the simulation of SWV in the Community Earth System Model, version 1 with the Whole Atmosphere Community Climate Model as its atmospheric component [CESM1(WACCM)]. CESM1(WACCM) generally tends to simulate a SWV maximum over the central Pacific Ocean, but this bias is largely improved in the high vertical resolution version. The high vertical resolution model with increased vertical layers in the UTLS is found to have a less stratified UTLS over the central Pacific Ocean compared with the low vertical resolution model. It therefore simulates a steepened potential vorticity gradient over the central Pacific Ocean that better closes the upper-level anticyclone and confines the SWV within the enhanced transport barrier.

1. Introduction

Both satellite and aircraft measurements show that tracer constituents exhibit localized extrema in the upper troposphere lower stratosphere (UTLS) over the Asian and North American monsoon regions during boreal summer, such as maxima of tropospheric species-like methane (Park et al., 2004), carbon monoxide (CO; Garny & Randel, 2016; Li, Jacob, et al., 2005; Li, Jiang, et al., 2005; Pan et al., 2016), and stratospheric water vapor (Dessler & Sherwood, 2004; Gettelman et al., 2004; Milz et al., 2005; Park et al., 2007; Rosenlof et al., 1997; Randel et al., 2015, 2001; Zhang et al., 2016), and minima of stratospheric species-like ozone (Gettelman et al., 2004; Park et al., 2008, 2007; Randel & Park, 2006; Randel et al., 2001). Among these chemical constituents in the UTLS, stratospheric water vapor (SWV) is important due to not only its radiative forcing on surface climate (Forster & Shine, 1999; Maycock et al., 2013; Solomon et al., 2010) but also its chemical effects on stratospheric ozone (Dvortsov & Solomon, 2001) and chlorine activation reactions (Anderson et al., 2012; Solomon et al., 2016). The importance of a realistic representation of the SWV over the Asian summer monsoon region in atmospheric models has been emphasized in simulating troposphere-stratosphere exchange correctly (Bannister et al., 2004; Dethof et al., 1999; Ploeger et al., 2013). Additionally, chemical species-like SWV also provide a complementary perspective on the upper-level monsoon circulation dynamics (Garny & Randel, 2013; Park et al., 2009; Ryu & Lee, 2010). However, models perform poorly in terms of their simulation of SWV (Jiang et al., 2012; Takahashi et al., 2016). Considerably large model biases in the simulations of SWV are found among models that participated in the Phase 5 of Coupled Model Intercomparison Project (CMIP5). There exists both wet and dry biases, ranging from 1% to about 200% at 100 hPa based on the multiyear mean vertical profiles of H_2O in CMIP5 models. Eight out of 19 CMIP5 models evaluated in Jiang et al. (2012) differ from the observed SWV at 100 hPa by more than 30%.

Previous studies have investigated the dynamical processes influencing the SWV over the Asian summer monsoon regions. It has been suggested that chemical tracers vertically transported by convection over the monsoonal region can reach the convective outflow level near 12 km (Folkins et al., 2000; Gettelman & Forster, 2002), and part of them are lifted subsequently by slow upward motion to 100 hPa and above (Park et al., 2008, 2009, 2007; Uma et al., 2014). As demonstrated in model experiments of Bergman et al. (2013) and Pan et al.

(2016), air parcels likely enter the UTLS through a vertical conduit between the center of the Asian monsoon anticyclone (AMA) and the strongest convective activity and are then circulated but confined within the monsoon anticyclonic flows associated with steepened geopotential height and potential vorticity (PV) gradients (Dethof et al., 1999; Dunkerton, 1995; Jackson et al., 1998; Park et al., 2007; Ploeger et al., 2017, 2015). The promoted gradients are characterized as a barrier to suppress horizontal transport across gradients (Bergman et al., 2013; Garny & Randel, 2013; Li et al., 2005; Park et al., 2008; Ploeger et al., 2017, 2015; Randel & Park, 2006; Rosenlof et al., 1997) and confine the slowly rotating air parcels within the AMA.

Both observational and modeling studies have been done to investigate the effects of monsoon convection on SWV. Dessler and Sherwood (2004) and Schwartz et al. (2013) proposed that the penetration by overshooting deep convection contributes to a wetter tropopause, implying that the monsoon deep convection susceptibly has a moistening effect in the UTLS. However, overshooting convection occurs irregularly, and the prominent center of deep convection is not colocated with but rather on the southeastern side of the SWV maximum (see Figure 2 in Park et al. (2007) and Figure 2a in Randel et al. (2015)). These facts cast doubts on this mechanism. Recently, Wright et al. (2011) and Randel et al. (2015) suggested that the large-scale circulation and the temperature on the southern side of the AMA play a dominant role in controlling the SWV over the Asian summer monsoon region, and in particular, they found that the stronger (weaker) the convection, the colder (warmer) the subtropical temperature, the dryer (wetter) the SWV at 100 hPa. This serves as a dehydration mechanism, which is governed by adiabatic cooling during the convection-driven upwelling and subsequent freezing out following the Clausius-Clapeyron relationship. The linear regression analysis between circulation and SWV variations at 100 hPa in observations shows an anomalous upper-level anticyclonic flow pattern during anomalous dry events, implying that dry UTLS is accompanied by an intensified AMA, which corresponds to a stronger monsoonal convection (Gill, 1980; Rodwell & Hoskins, 1996), and vice versa. Randel et al. (2015) suggested that the temperature on the southern side of the AMA acts as a key link between the large-scale circulation and SWV. Schoeberl and Dessler (2011) and Kim et al. (2013) commented that small temperature variance can significantly affect the SWV, that is, a 4°K temperature change at 100 hPa could induce 60% (approximately 3 ppmv) variation of SWV following the Clausius-Clapeyron relationship. Both radiosonde measurements and model experiments indicate that convection exerts a cooling effect in the AMA region, which is associated with radiative cooling, cold air entrainment, and equatorial wave propagation in the upper troposphere (Gage et al., 1991; Gettelman & Forster, 2002; Highwood & Hoskins, 1998; Kim et al., 2018; Kuang & Bretherton, 2004; Norton, 2001; Park et al., 2007; Randel & Wu, 2005; Sherwood et al., 2003; Tsuda et al., 1994; Zhou & Holton, 2002). Therefore, the dehydration mechanism suggests that enhanced convection substantially dehydrates the air, as opposed to the moistening effect by overshooting convection.

Previous studies mostly examined the simulations of area-averaged SWV (Hardiman et al., 2015; Inness et al., 2001; Roeckner et al., 2006), generally in the deep tropics; however, a detailed investigation of the spatial distributions over the summer monsoon regions has not yet been performed. More specifically, the questions we aim to address in this study are as follows: (1) How good is SWV simulated in the Whole Atmosphere Community Climate Model (WACCM) experiments? (2) What causes the biases in the simulation of SWV? and (3) Several studies have emphasized the importance of increased model vertical resolution in capturing many critical UTLS processes (Abalos et al., 2013; Charlton-Perez et al., 2013; Gettelman et al., 2010; Inness et al., 2001; Kim et al., 2013; Lindzen & Fox-Rabinovitz, 1989; Pope et al., 2001; Roeckner et al., 2006; Richter et al., 2014; Wang et al., 2013); therefore, will increased model vertical resolution promote an improved representation of the monsoon signature on the SWV? The remainder of the paper is organized as follows: section 2 describes the model experiments and observational data; section 3 presents the model evaluation of both SWV and CO and proposes the underlying mechanism for the model biases. Summary and discussions are in section 4.

2. Data and Methods

2.1. WACCM Experiments

The Community Earth System Model version 1 (CESM1; Hurrell et al., 2013 WACCM includes interactive atmosphere, ocean, land, and sea ice components (Marsh et al., 2013; Mills et al., 2016). WACCM is one of the high-top state-of-the-art chemistry-climate models, integrating the atmospheric physics and chemistry from the surface to nearly 140 km. Two model configurations with almost identical model setups but different vertical resolutions are examined in this study: CESM1(WACCM)-L70 (hereafter L70) with 70 vertical levels and CESM1(WACCM)-L110 (hereafter L110) with 110 vertical levels, both with horizontal resolution of 0.95° latitude × 1.25° longitude (~100 km). The vertical resolution in the midtroposphere and lower stratosphere is

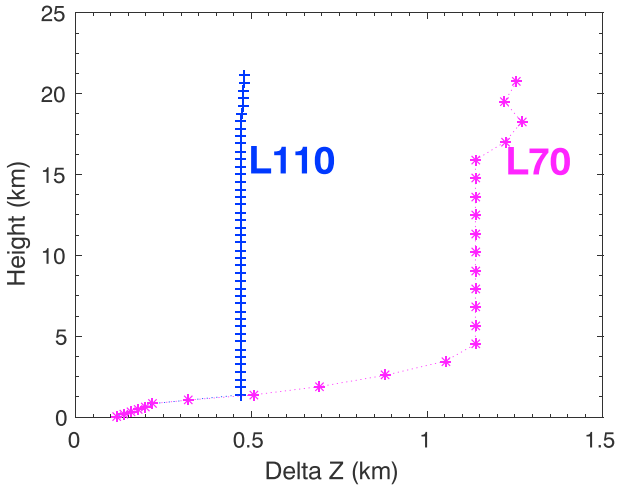

Figure 1. Vertical grid spacing in kilometers as a function of height used in the Community Earth System Model version 1(Whole Atmosphere Community Climate Model) simulations with 70 vertical levels (asterisks) and 110 vertical levels (plus signs) from the surface to 50 hPa. L70 = 70 vertical levels; L110 = 110 vertical levels.

about 1.2/0.5 km in the L70/L110 (see Figure 1). The two models include improved physics processes, convective parameterizations, and fully interactive chemistry modified from the Community Atmosphere Model, version 5 (Mills et al., 2016; Neale et al., 2010). The orographic and nonorographic gravity waves drag (GWD) parameterizations are almost identical in L70 and L110 following Richter et al. (2010). The parameter tuning of GWD is modified as a result of refined vertical resolution following the Stratosphere-troposphere Processes And their Role in Climate Quasi-Biennial Oscillation initiative protocol (Butchart et al., 2018). L70 and L110 are coupled to the biogeophysical and biogeochemical parameterizations and numerical implementation of version 4.5 of the Community Land Model (Oleson et al., 2013). Most of the details about L70 are documented in Mills et al. (2017), and the details of L110 are described in Butchart et al. (2018). The climatological simulations averaged over June, July, and August spanning the range from 1979 to 2014 in both models are compared.

Both the L70 and L110 are fully coupled ocean-atmosphere experiments, and the difference between the two reveals the impact due to solely vertical resolution. In addition to the coupled model, L110 forced with prescribed sea surface temperatures and sea ice properties based on the Atmospheric Model Intercomparison Project (AMIP) experiment (Taylor et al., 2012) is also examined here. Additionally, two experiments subject to the same settings but with different boundary conditions using CESM1(WACCM4), which participated in the Chemistry Climate Model Initiative (CCMI) experiments (Eyring et al., 2013; Morgenstern et al., 2017) with nudged Quasi-Biennial Oscillation, are used. One integration is an AMIP-style (CCMI-AMIP) run, whereas the other is a coupled ocean-atmosphere run (CCMI-Coupled). WACCM4 has a horizontal resolution of 1.9° latitude × 2.5° longitude and 66 layers in the vertical (Garcia et al., 2017; Marsh et al., 2013; Tilmes et al., 2016) and is the high-top version of Community Atmosphere Model, version 4. The information of WACCM experiments with different configurations evaluated in this study are summarized in Table 1.

2.2. Microwave Limb Sounder Water Vapor

We analyze the water vapor measurements derived from the Aura Microwave Limb Sounder (MLS) version 4.2 level 2 products (Livesey et al., 2018). The main development in MLS v4.2 water vapor retrievals is an improved cloud detection methodology. MLS data are available from 2004 to present. Here we use the retrievals spanning the range from 2005 to 2014 to evaluate the performance of CESM1(WACCM) models. MLS provides H_2O (water vapor volume mixing ratio in parts per million by volume) with vertical resolution around 3 km in the UTLS. The uncertainties in H_2O measurements are about 20% near the upper troposphere (215 hPa) and 10% at the UTLS (100 hPa) in the tropics and midlatitudes (Jiang et al., 2012, 2015).

Table 1
Characteristics of the Models Analyzed in the Study

Model	Vertical layers	Horizontal resolution	Period spanned
CESM1(WACCM)-L70	70	0.95° latitude × 1.25° longitude	1979–2014
CESM1(WACCM)-L110	110	0.95° latitude × 1.25° longitude	1979–2014
L110-AMIP	110	0.95° latitude × 1.25° longitude	1979–2014
CCMI-AMIP	66	1.9° latitude × 2.5° longitude	1979–2014
CCMI-Coupled	66	1.9° latitude × 2.5° longitude	1979–2014
CESM1(WACCM4)	66	1.9° latitude × 2.5° longitude	1950–2006
SC-WACCM4	66	1.9° latitude × 2.5° longitude	1950–2008
SD-WACCM4	88	1.9° latitude × 2.5° longitude	2005–2010

Note. CESM1 = Community Earth System Model version 1; WACCM = Whole Atmosphere Community Climate Model; L70 = 70 vertical levels; L110 = 110 vertical levels; AMIP = Atmospheric Model Intercomparison Project; CCMI = Chemistry Climate Model Initiative; SC = specified chemistry; SD = specified dynamics.

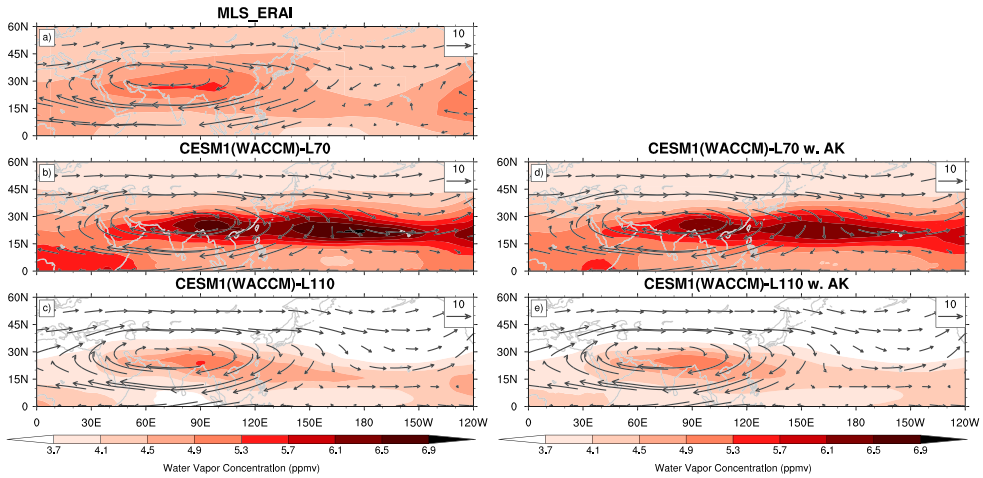

Figure 2. The colors show the summertime SWV (ppmv) at 100 hPa from (a) MLS, (b) L70, (c) L110, (d) L70 weighted by AK, and (e) L110 weighted by AK during 2005–2014, overlaid with the averaged horizontal winds (m/s) in vectors during 2005 to 2014 at that level. Winds in (a) are from ERAI and (b, d) and (c, e) are from L70 and L110, respectively. SWV = stratospheric water vapor; MLS = Microwave Limb Sounder; ERAI = ERA-Interim; L70 = 70 vertical levels; CESM1 = Community Earth System Model version 1; WACCM = Whole Atmosphere Community Climate Model; L10 = 110 vertical levels; AK = averaging kernel.

2.3. ERA-Interim Meteorological Analyses

We use both daily and monthly meteorological analyses from ERA-Interim (ERAI) reanalysis (Dee et al., 2011), including temperature and wind fields with horizontal resolution of 1° latitude × 1° longitude. Monthly ERAI data during the overlapping time period as the WACCM experiments (1979–2014) are analyzed to validate the model simulations of temperature and circulations. Both daily and monthly ERAI data of PV, temperature, and circulations from 2005 to 2014 overlapping with MLS data are used for composite analysis.

3. Results

The analyses are mostly performed on the simulations at 100-hPa level. MLS observations show that the localized SWV maxima during boreal summer are primarily at 100 hPa (Randel et al., 2015; Zhang et al., 2016), which is confined by the AMA effectively near 100 hPa (Randel & Park, 2006). Furthermore, Randel et al. (2015) found that the climatology and variability of SWV were nearly identical on isentropic versus pressure levels. Therefore, we choose the model levels nearest to 100 hPa in order to avoid uncertainties due to interpolation, specifically 103 hPa in L70 and 102 hPa in L110. If not specified, the pressure levels in this study refer to the nearest model levels. Temperature fields nearest to 200 hPa are also explored.

3.1. Simulation of Stratospheric Water Vapor Over the Asian Summer Monsoon Region

The boreal summer (June, July, and August) climatological distributions of 100-hPa water vapor in MLS data and the L70/L110 simulations during 2005–2014 are shown in Figure 2. The model results are not sensitive to the averaging time period (similar results are found during 1979–2014; not shown). The 100-hPa horizontal circulation averaged during 2005–2014 is also shown in Figure 2. The circulation in Figure 2a shows the equatorial easterly, subtropical westerly, and the relatively strong meridional flows acting together to encompass the AMA center. The maxima SWV values (~5.3 ppmv) at 100 hPa are clustered over the zonally elongated domains of 20–35°N, 40–120°E, strongly coherent within the AMA but distant from the deep convection center in the Southeast Asia. The localized SWV maximum in observations exhibits a strong monsoon dynamical signature.

Figures 2b and 2c show the multiyear mean SWV and circulation simulated in L70 and L110, respectively. To better highlight the model performance as compared with observations, Figures 3a and 3b show the percentage differences in L70 and L110 relative to MLS observations. It is noteworthy that, in L70 (shown in Figure 2b), the maximum (~6.9 ppmv) is located over the central Pacific (170°E to 170°W), and the secondary maximum (~6.5 ppmv) is located within the AMA. Although the overall magnitude of SWV over the continent is well captured in L70, the wet bias over the central Pacific (~50%) significantly exceeds the 10% range of uncertainty in MLS (shown in Figure 3a). The bias in SWV in L70, in particular that the maximum is located over the

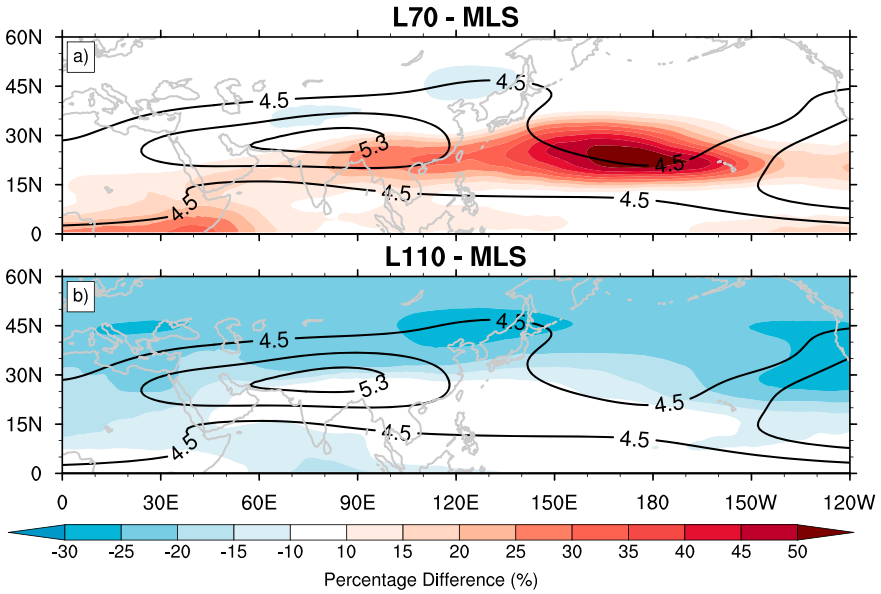

Figure 3. Color shadings show the percentage difference in (a) L70 and (b) L110 with respect to the MLS measurements during JJA 2005–2014. The black contours are the MLS SWV as in Figure 2a with contour interval of 0.4 ppmv. L70 = 70 vertical levels; L110 = 110 vertical levels; JJA = June, July, and August; MLS = Microwave Limb Sounder; SWV = stratospheric water vapor.

ocean rather than the continent, is surprising given the current understanding of the AMA dynamics (Qu & Huang, 2015; Rodwell & Hoskins, 1996) and the observed linkage between the AMA and SWV (Randel et al., 2015). Compared with L70, L110 with increased vertical resolution and refined GWD parameterizations shows a significant improvement in the simulation of SWV, particularly in terms of its spatial distribution. Figure 2c displays a maximum of about 5.3 ppmv located within the AMA in L110, which is similar to observations (Figure 2a). Comparing to the SWV in MLS, L110 has a dry bias (~25%) poleward of 30°N (see Figure 3b). The meridional velocity on the eastern flank of the AMA decreases sharply from the continent to the ocean, which helps the anticyclonic flows close better in L110.

The effects of the averaging kernels (AKs) on the simulated SWV at 100 hPa are checked. The details about the MLS AKs are discussed in Livesey et al. (2018). Figure S1 in the supporting information displays the equatorial MLS v4.2 AK that we applied to the simulations. Figures 2d and 2e show the SWV convolved with the AK from L70 and L110, respectively. The weighted SWV shown in Figures 2d and 2e stay very close to what we have seen in Figures 2b and 2c, which indicates that the influence of AK is small in the subtropics.

In addition to the SWV difference, discrepancies are also found in the temperatures and circulations in L70 as shown in Figure 4a with respect to the summer climatology (2005–2014) in ERAI reanalysis. There is a warm bias over the continent and a cold bias over the central Pacific Ocean (boxed regions in Figure 4; 15–30°N, 170°E to 170°W) in L70, and the anomalous westerlies exist along the entire subtropics in L70 as compared with those in ERAI reanalysis and L110 (Figures 4a, 7a, 7b, and 9a). The eastern branch of the AMA is found extending eastward to the central Pacific Ocean, which we claim is responsible for the poor simulation of the SWV (to be discussed). The biases of temperatures, especially the cold center over the central Pacific Ocean, are reduced in L110 as compared with L70 (see Figure 4b).

Though both L70 and L110 presented above are coupled models, the side-by-side comparisons of coupled runs with their atmosphere-only counterparts indicate that the performance of simulated SWV and circulation around 100 hPa is insensitive to boundary conditions. As depicted in Figure S2, the simulation of AMIP-style L110 (Figure S2a) closely resembles the structure of coupled runs (Figure S2c) and observations. Compared with coupled L110, the dry bias over the continent is improved and the AMA is better closed in AMIP-style L110. Meanwhile, the common deficiencies can be seen in both the AMIP-style (Figure S2b) runs and coupled runs (Figure S2d) from the WACCM4 CCMI experiments, notably with the SWV maximum shifted eastward and circulations extended to the Pacific Ocean. This suggests that the differences in SWV simulations are likely

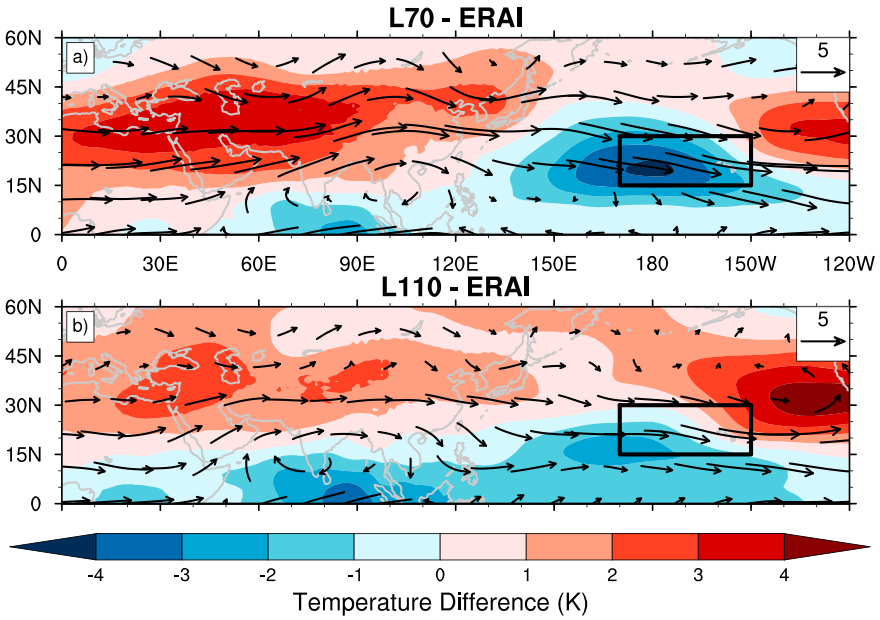

Figure 4. Color shadings and vectors represent the difference in the 100-hPa temperature (K) and the difference in the 100-hPa horizontal wind fields (m/s) in (a) L70 and (b) L110 with respect to the ERAI reanalysis from 2005 to 2014. The black boxes outline the domains (15–30°N, 170°E to 170°W) in which large temperature differences are found. L70 = 70 vertical levels; ERAI = ; ERA-Interim; L110 = 110 vertical levels.

due to the model vertical resolution and refined GWD parameterizations and not to differences in boundary conditions.

Moreover, other configurations of WACCM4 that are available are also studied (see Table 1 and Figure S3), that is, CESM1(WACCM4) in the CMIP5 archive, specified chemistry (SC)-WACCM4 (Smith et al., 2014), and specified dynamics (SD)-WACCM4 (Kunz et al., 2011; Lamarque et al., 2012). The specific humidity (kg/kg) outputs from these models are converted to the water vapor volume mixing ratio by multiplying 1.61 (ppmv/ppm). The CESM1(WACCM4) (Figure S3a) and SC-WACCM4 (Figure S3b) look remarkably similar to each other, but both unrealistically simulate the SWV maximum over the Pacific Ocean. The SD-WACCM4 is nudged toward the Goddard Earth Observing System, Version 5 meteorological analysis (i.e., horizontal wind and temperature fields) of NASA's Global Modeling and Assimilation Office (Arnone et al., 2014; Lamarque et al., 2012; Rienecker et al., 2011). The SD-WACCM4 similarly shows a maximum of SWV over the central Pacific Ocean (see Figure S3c), and this bias is also found in the Modern-Era Retrospective Analysis for Research and Applications (MERRA) reanalysis specific humidity (not shown). The biased SWV in SD-WACCM4 is likely attributed to the unreliable temperature in MERRA reanalysis above 300 hPa (Jiang et al., 2012, 2015; Tian et al., 2013). The temperature differences of MERRA compared with ERAI in the UTLS can be up to 2°K (see Fueglistaler et al., 2013; Figure C3) and Bosilovich (2015, Figures 3 - 5). To sum up, the discrepancies are commonly found in WACCM experiments with different configurations.

In section 3.2, we will focus on the L70 and L110 and will provide a possible mechanism to explain the differences between the two, specifically the magnitude and spatial pattern associated with the Asian summer monsoon circulation.

3.2. Mechanisms Underlying Differences in High and Low Vertical Resolution Models

3.2.1. Differences in Temperatures in High and Low Vertical Resolution Models

Since the SWV relies strongly on the UTLS temperature, we start by analyzing the temperatures between the high and low vertical resolution models. Figures 5a and 5b show the temperature differences in L70 and L110 at 100 and 200 hPa, respectively. It is noteworthy that salient temperature difference (~1.5–3 K) between L70 and L110 lies over the central Pacific Ocean at 100 hPa (see Figure 5a). Similar patterns are found averaging from 1979 to 2014 (not shown). In L70, it is relatively cold over the subtropical central Pacific (boxed regions in Figure 5; 15–30°N, 170°E to 170°W) compared to L110. The cold bias is accentuated at higher levels above 100 hPa. However, the temperature difference in the subtropics shows the opposite sign in the levels below

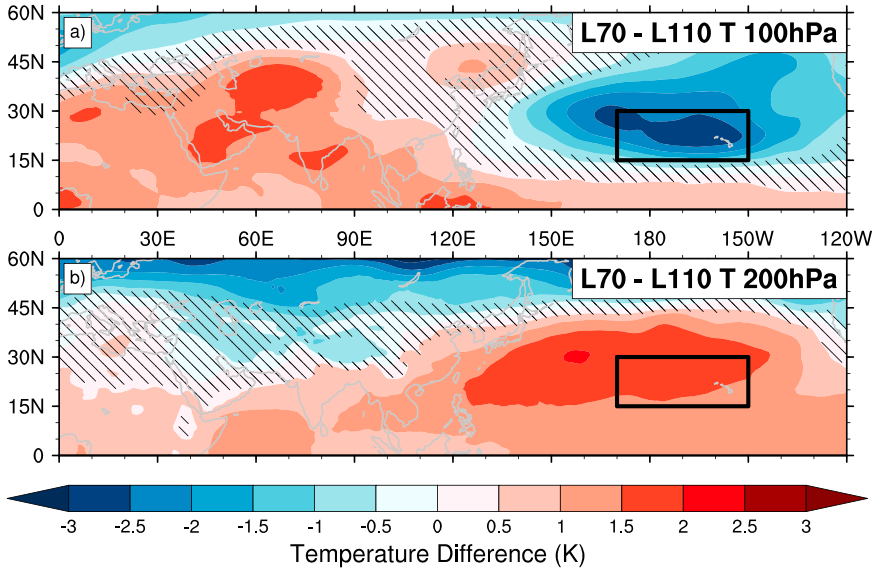

Figure 5. Color shadings represent the temperature difference (K) in L70 versus L110 at (a) 100 hPa and (b) 200 hPa from 2005 to 2014. The hatching in the right indicates where the differences are not statistically significant at the 95% confidence level using the Student's *t* test. The black boxes are the same as in Figure 4. L70 = 70 vertical levels; L110 = 110 vertical levels.

140 hPa (see 200 hPa as an example, shown in Figure 5b). The zonal mean temperature differences between the two models in a longer time period (1979–2014) are shown in Figure 6a. The dipole structure in the temperature difference suggests that the lower vertical resolution model is relatively warm in the free troposphere and cool in the lower stratosphere, which is a robust result as found in other studies (Inness et al., 2001; Pope et al., 2001; Roeckner et al., 2006; Richter et al., 2014). Similar temperature bias pattern can be found in L70 relative to ERAI (see Figure 6b). But this bias is largely reduced in L110 (see Figure 6c). In the Northern Hemisphere subtropics, the warm anomaly in L70 in the troposphere is largely due to the warm anomaly over the Pacific Ocean and the cold anomaly in the lower stratosphere is dominated by that over the Pacific Ocean.

First, we explain the zonal mean temperature difference in the troposphere between L70 and L110 models. To do that, we compare the climatological outgoing longwave radiation and pressure velocity (ω) at 445 hPa between the two models. As shown in Figure S4, weaker outgoing longwave radiation associated with stronger vertical ascent is seen in the western Pacific in L70, indicating that the model with coarser vertical resolution has stronger convective activities. Richter et al. (2014) also documented that the model with higher vertical resolution can reduce the positive bias of precipitation over the Asian summer monsoon region. In order to quantify the total diabatic heating (including radiative heating, sensible heating, latent heating, and eddy heating flux) released to the environment, the climatological apparent heat source Q1, which is the residual of the heating budget of resolvable variables, is calculated following equation (S1; details in Text S1

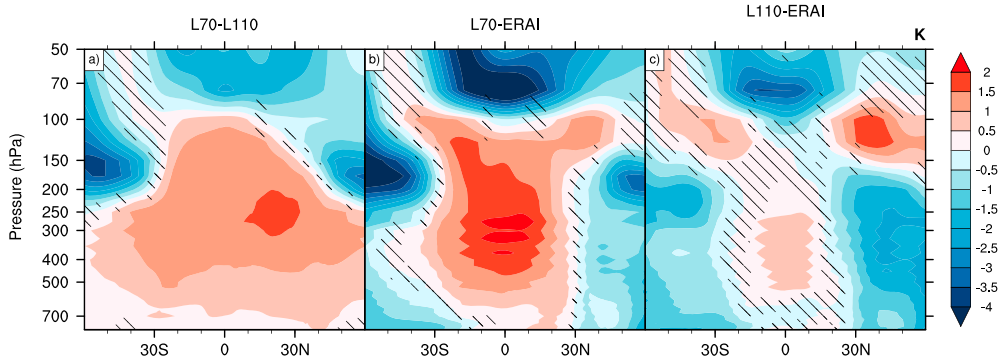

Figure 6. Zonal mean temperature difference (K) in (a) L70 and L110, (b) L70 and ERAI, and (c) L110 and ERAI. The hatching is the same as in Figure 5. L70 = 70 vertical levels; L110 = 110 vertical levels; ERAI = ERA-Interim.

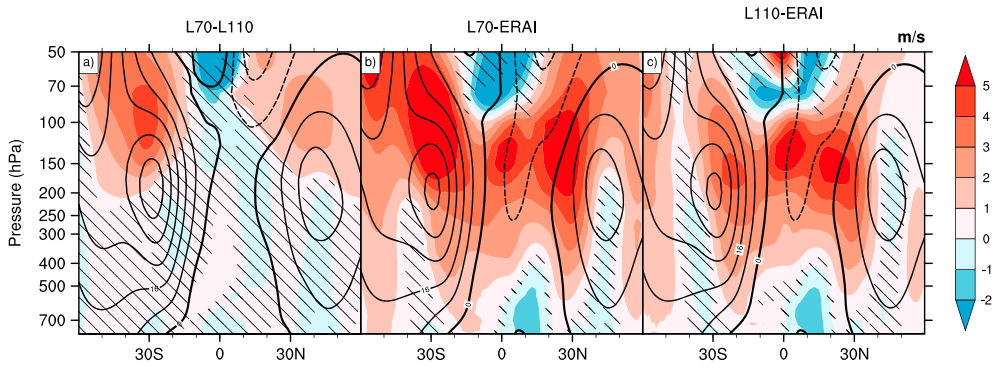

Figure 7. Difference in zonal mean zonal wind (m/s, color shading) between (a) L70 versus L110, (b) L70 versus ERAI, and (c) L110 versus ERAI, respectively. The black contours with contour interval of 8 m/s represent the climatological zonal mean zonal wind in L110 in (a) and the zonal mean zonal wind in ERAI in both (b) and (c). Solid contours are for positive values, dashed for negative, and thick solid for zero. The hatching is the same as in Figure 5. L70 = 70 vertical levels; L110 = 110 vertical levels; ERAI = ERA-Interim.

in the supporting information). As shown in Figure S5, the apparent heating averaged over the Pacific Ocean (170°E to 170°W) is stronger in the midtroposphere between 10°N and 20°N due to stronger convective activities in L70. Therefore, the warmer upper troposphere over the Pacific Ocean can be explained by the stronger heating associated with stronger convective activities in the coarser vertical resolution model.

In stark contrast, relatively strong cold bias appears in the lower stratosphere in L70 compared with L110 (Figure 6a) and is seen over the Pacific Ocean (Figure 5a). Here we attribute the cold anomaly in the lower stratosphere in L70 to stronger upwelling (see Figure S6). The wave-driven large-scale ascent in the tropical tropopause layer accompanied by adiabatic cooling is considered to play a dominant role in driving the lower-stratospheric temperature. The upwelling is forced by both the extratropical and tropical waves (Randel & Jensen, 2013). Extratropical stratospheric pumping and downward control mechanism associated with wave dissipation in the subtropics could induce an upwelling in the tropical lower stratosphere (Chen & Sun, 2011; Haynes et al., 1991; Garcia & Randel, 2008; Garny et al., 2011; Plumb & Eluszkiewicz, 1999; Randel & Jensen, 2013; Reid & Gage, 1996; Taguchi, 2009), and the dissipation of waves is proportional to the strength of the zonal mean zonal wind (Andrews et al., 1987; Calvo et al., 2010). Figure 7a shows the differences in zonal mean zonal wind in the two models, and L70 has a stronger (~2 m/s) and slightly equatorward shifted subtropical jet compared with L110. This is consistent with the larger meridional temperature gradient in the tropics (Figure 6a) and also the overall larger SWV (Maycock et al., 2013) in L70. Compared with ERAI, there is an overall westerly bias prevailing in the UTLS in both model simulations but it becomes reduced in the L110 (see Figures 7b and 7c).

To explain the difference in stratospheric temperature between L70 and L110, we calculate the transformed Eulerian mean vertical velocity $\bar{w}^*$ using monthly variables following (Andrews et al., 1987; details in Text S2 in the supporting information). Figure S6 shows the vertical residual velocity $\bar{w}^*$ difference between L70 and L110. The tropical ascent and extratropical descent can be seen in L110 climatology. In L70, there is an anomalous ascent in the tropics in general, likely due to enhanced subtropical jet, which contributes to the cold anomaly in the lower stratosphere (Andrews et al., 1987; Calvo et al., 2010). Besides, several other processes might also contribute to the increased ascent in L70. The intensification of both Rossby wave-driven and the equatorial wave-driven upwelling associated with the enhanced convective heating could contribute to the stronger mean ascent in the UTLS in L70 (Boehm & Lee, 2003; Norton, 2006; Ryu & Lee, 2010). Additionally, the dipole temperature structure is accompanied by an upward shift of the cold point tropopause in coarser vertical resolution model (Abalos et al., 2013), which could also contribute to the anomalous cooling in the lower stratosphere through the difference in the established radiative equilibrium between L70 and L110 (Kuang & Bretherton, 2004). The anomalous adiabatic cooling induced by the enhanced upwelling is compensated by stronger radiative heating in L70 (not shown). Ackerman et al. (1988) and Gage et al. (1991) suggested that the presence of ice particles, thin cirrus, and aerosols is a possible candidate for the larger heating rate in the lower stratosphere. In L70, we also find more frequent high clouds (not shown), which is likely to balance the anomalous adiabatic cooling induced by upwelling.

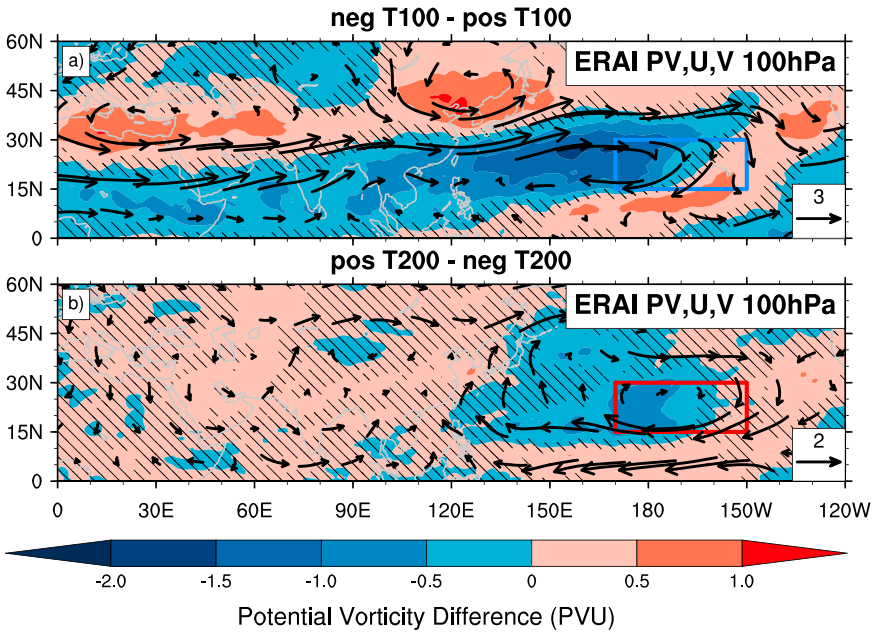

Figure 8. Difference in the composited 100-hPa PV (color shadings) and winds (m/s; vectors) for the temperatures averaged in the box (15–30°N, 170°E to 170°W) above the central Pacific for (a) cold and warm temperature days at 100 hPa and (b) warm and cold temperature days at 200 hPa. The hatching is the same as in Figure 5. PV = potential vorticity; ERAI = ERA-Interim.

3.2.2. Differences in SWV Magnitude

Here we use the above analysis of the difference in temperatures between L70 and L110 to explain the difference in the magnitude of SWV. As discussed in section 1, Randel et al. (2015) documented that the dehydration primarily occurs on the equatorial flank of the AMA and more SWV is associated with warmer temperature at 100 hPa. Figures S7a and S7b show the regression coefficient of the SWV variations in the box region (20–40°N, 40–140°E) regressed onto the temperatures at 100 hPa in L70 and L110, respectively. The patterns resemble that (see Randel et al., 2015; Figure 8) and show a warm temperature anomaly on the equatorward flank of the AMA associated with a wet anomaly of SWV, indicating that both L70 and L110 are able to reproduce the dehydration mechanism. As shown in Figure 5a, the warmer temperature is found in the equatorial flank of the AMA at 100 hPa in L70, which is consistent with the relatively wet SWV in the domain of interest (see Figure 3).

However, we note here that the warmer temperature over the continent at 100 hPa in L70 is not likely a result of stronger convective activities since a stronger convection is associated with a colder tropopause temperature within the AMA region (Park et al., 2007; Randel et al., 2015). Instead, other factors such as difference in vertical resolution with refined GWD parameterizations may play a role.

Additionally, as shown in Figure 5a, large difference in UTLS temperature over the central Pacific Ocean is found between the two models with L70 colder than L110. The evident cold center is collocated with the unrealistic SWV maximum in L70, which rules out the possibility of direct vertical transport from below according to the dehydration mechanism. Instead, we argue that it is the UTLS temperature difference over the Pacific Ocean that plays a critical role in the simulation of the AMA and SWV spatial distribution (to be discussed next).

3.2.3. Differences in SWV Spatial Distribution

As shown in Figure 2b, conspicuous wet bias of simulated SWV is found over the central Pacific Ocean in L70 and it is a common model deficiency as found in a suite of WACCM experiments (Figures S2b, S2d, and S3). As shown in the 3-D trajectory runs in Randel and Park (2006), most of the particles released on the isobaric surfaces within the AMA remain inside the domain after several weeks, and a relatively small fraction of particles is transported eastward outside. The AMA associated with the Asian monsoon deep convection has a large dynamical variability (Gill, 1980; Jin & Hoskins, 1995; Popovic & Plumb, 2001), and therefore, it is challenging to locate the north-south boundary of the horizontal transport barrier for UTLS chemical species (Garny & Randel, 2013; Ploeger et al., 2015). For our study, one candidate that likely contributes crucial parts in

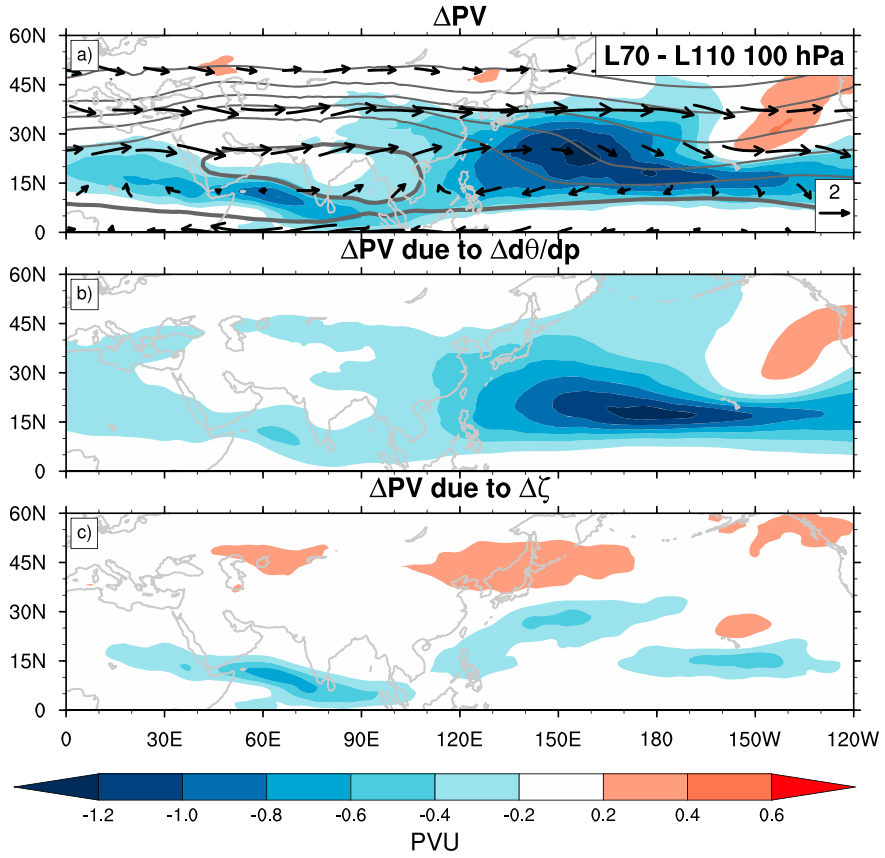

Figure 9. (a) Difference of PV (color shadings) and winds (m/s; vectors) between L70 and L110 at 100 hPa. The gray contours represent the climatological PV in L110 (contour interval: 2 PVU). The thick gray line indicates 2 PVU surface. The decomposition of the PV difference (L70 minus L110) into the contributions (b) due to the difference in stratification (i.e., $-g(f+\zeta)\delta(\frac{\partial\theta}{\partial p})$) and (c) due to the difference in horizontal circulation (i.e., $-g\delta(f+\zeta)(\frac{\partial\theta}{\partial p})$).

confining the SWV within the anticyclonic flow, specifically in the east-west boundary, is the UTLS temperature over the central Pacific Ocean.

The mechanism is proposed based on the compensation between the temperature anomaly and the PV anomaly. The negative PV anomaly is commonly used as an indicator for the intensity of the AMA (Bergman et al., 2013; Garny & Randel, 2013; Randel & Park, 2006). Small PV gradient inside the AMA indicates that the air is well mixed. Previous studies have emphasized the importance of the strong PV gradient at the edge of the AMA on suppressing the cross-gradient advection and characterizing the horizontal transport barrier (Ploeger et al., 2015). Composite analyses using ERAI reanalysis are conducted here in order to illustrate the linkage between the temperature and PV gradient. As discussed in section 3.2.1, conspicuous temperature differences are found over the central Pacific region (15–30°N, 170°E to 170°W) in the UTLS between L70 and L110 with different signs at 100 and 200 hPa. First, we show the linkage between 100-/200-hPa temperature anomalies and anomalous PV/winds at 100 hPa using ERAI reanalysis data. Daily temperature and PV from the ERAI reanalysis spanning the range of 10 years (from 2005 to 2014) are employed. The monthly data show similar results (not shown here). We define the warm (cold) events as the days when the area-averaged temperature over the noted domain (15–30°N, 170°E to 170°W) is higher (lower) than the 10-year average value during summer months at each pressure level. Our analyses are based on compositing 100-hPa PV for the warm events and cold events at 100 and 200 hPa, respectively. Figure 8a shows the composite difference of 100-hPa PV between the 100-hPa cold and warm events. The sign of the PV anomaly is such that the low PV anomaly expanding eastward occurs in association with the colder than normal central Pacific temperature at 100 hPa with uniformly stronger subtropical westerlies (~2 m/s) and an anticyclonic flow anomaly over the western Pacific Ocean, which is directly analogous to that in L70 (see Figure 9a). It indicates that the relatively cold temperature in L70 at 100 hPa compared with L110 is related to the negative PV anomalies. Figure 8b

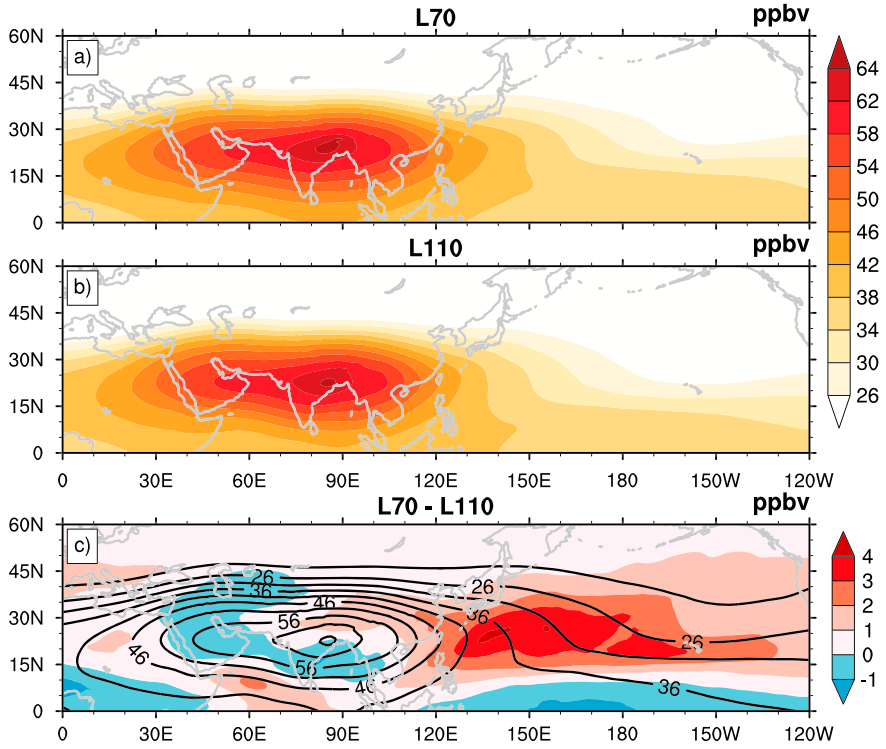

Figure 10. The colors show the summertime horizontal structures of CO (ppbv) from (a) 103 hPa L70 and (b) 102 hPa L110 averaged over 1979 to 2014. (c) Colors show the CO difference (ppbv) between L70 and L110 with CO in L110 (black contours).

shows the composite difference of 100-hPa PV between the 200-hPa warm and cold events. The anomalous anticyclonic flow and negative PV are found on top of the warm temperature region over the central Pacific, and this is analogous to that in L70 as well. Therefore, both the cold bias at 100 hPa and the warm bias at 200 hPa in L70 lead to low PV anomaly extending to the Pacific Ocean and further diminish the PV gradient on the eastern flank of the AMA.

To further quantify the cause of the negative PV anomaly over the Pacific Ocean in L70 compared with L110, we decompose the PV difference into the contributions due to stratification difference and due to relative vorticity difference as follows (Wu & Shaw, 2016):

$$\delta \mathrm{PV} \approx \underbrace{-g(f+\zeta)\delta\left(\frac{\partial\theta}{\partial p}\right)}_{\text{stratification difference}} \underbrace{-g\delta(f+\zeta)\left(\frac{\partial\theta}{\partial p}\right)}_{\text{relative vorticity difference}} \tag{1}$$

where δ indicates the difference between the L70 and L110, g is the gravitational acceleration, f is the Coriolis parameter, and ζ is the relative vorticity. The sum of the decomposition following the right-hand side of equation (1) is about equal to the left-hand side (not shown). Compared with L110, L70 has a negative PV anomaly over the central Pacific Ocean (Figure 9a). We find that, in L70, both the less stratified UTLS (Figure 9b) and, to a lesser extent, the anomalously anticyclonic circulation (Figure 9c) contribute to the negative PV anomaly over the Pacific Ocean and result in a relatively weak PV gradient on the eastern branch of the AMA (see Figure 9a) and thus a more leaky transport barrier in L70. Since SWV is highly sensitive to temperature, once SWV is extended to the relatively warm place over the Pacific Ocean as compared with the continent, it tends to stay there; thus, the maximum of SWV is seen over the Pacific Ocean in L70.

3.3. The Simulations of CO Over the Asian Summer Monsoon Region

Although this study focuses mostly on the simulations of the SWV, we also evaluate the simulated CO in the two models as complementary evidence. Since both the spatial pattern and magnitude of CO are less dependable on the temperature fields, it is highly controlled by the large-scale circulation. Overall, L70 and L110 are able to reproduce the localized maximum embedded within the AMA reasonably well (see Figures 10a

and 10b), which is consistent with the work by Pan et al. (2016), who examined the variability of CO and its linkage to the AMA in SD-WACCM4. However, compared with the simulation in L110, in L70, CO is not well isolated within the AMA and leaks out from the southeastern Asia to the central Pacific in the subtropics (see Figure 10c), which is highly collocated with the PV anomaly (shown in Figure 9a). But L70 has a more reasonable simulation of CO compared to water vapor, likely due to its less dependence in the UTLS temperature and relatively short lifetime. Therefore, we confirm that the UTLS temperature anomalies over the central Pacific are responsible for the model deficiency in the confinement of chemical constituents in L70.

4. Summary and Discussion

Our primary purpose of this study has been to examine the model performance in the simulation of SWV associated with the Asian summer monsoon and whether model vertical resolution affects the representation of SWV. We have found that the maximum of the simulated SWV is located over the central Pacific Ocean in most of the WACCM configurations, instead of over the Asian continent as in the MLS retrievals. The high vertical resolution model L110 with refined GWD parameterization, though displaying a dry bias on the poleward side, corrects the deficiency with SWV confined within the AMA and maximized over the continent.

Our results indicate that the temperature over the central Pacific Ocean is a significant factor in the representation of the Asian monsoon characters in the UTLS. We find that one of the improvements with increased vertical resolution and refined GWD parameterization lies in resolving the UTLS temperature more accurately, which is consistent with Richter et al. (2014). The relatively strong convection in L70 likely contributes to the warmer troposphere-cooler stratosphere dipole pattern. L110 with higher vertical resolution and refined GWD is capable of alleviating the cold bias above and the warm bias below 100 hPa over the central Pacific Ocean and therefore simulates a steepened PV gradient over the central Pacific Ocean that better closes the upper-level anticyclone and confines the SWV within the enhanced transport barrier.

Before concluding, possible caveats have to be noted. First, although L110 corrects the cold anomaly over the central Pacific Ocean, we did not explicitly address why but suspect that it is related to the stronger ascent occurring over the central Pacific Ocean. The observational evidence of the upward motion in the lower stratosphere occurring over central Pacific Ocean is documented in Gage et al. (1991). Second, the purpose of this study is to make use of the model experiments that are available and have a clean pair of low and high vertical resolution versions to examine the model performance of simulating SWV. However, to further test the robustness of the mechanism proposed in this study, we plan to extend the analysis to an ensemble of models that participated in the CCMI experiments in future work.

Previous studies have focused on the westward eddy shedding of the AMA and its role in chemical transport (Garny & Randel, 2016; Popovic & Plumb, 2001). Different from previous studies, our work emphasizes the importance of the eastern branch of the AMA in the confinement of chemical transport and the necessity to improve the representation of that in climate models. Despite the difference in simulated convection, it is the increased vertical resolution and refined GWD parameterization that improve the representation of the UTLS temperature and thus the anticyclone dynamics and SWV. The overall results demonstrate that models in general have biases in simulating SWV, which is likely associated with stronger westerlies and weaker PV gradient in the Northern Hemisphere subtropics. Our results demonstrate that model version with increased vertical resolution is able to correct these biases.

Acknowledgments
We are thankful to Kai Zhang and Alyn Lambert for their help in processing MLS data. We appreciate William J. Randel, Mijeong Park, Joowan Kim, Pengfei Zhang, and Ben Li for helpful discussion. We thank anonymous reviewers for their valuable comments, which helped to greatly improve the manuscript. The MLS averaging kernels were downloaded from https://mls.jpl.nasa.gov/data/ak/. The ERA-Interim meteorological data set was downloaded from http://apps.ecmwf.int/datasets/data/interim-full-daily/. The CESM project is supported by the National Science Foundation and the Office of Science (BER) of the U.S. Department of Energy. The National Center for Atmospheric Research is funded by the National Science Foundation. X. W. and Y. W. are supported by the National Science Foundation (NSF) [10.13039/100000001] grant AGS-1802248. Y. X. and Y. H. acknowledge funding from the Class G&C Program of the Canadian Space Agency (16SUASURDC).

References

Abalos, M., Randel, W., Kinnison, D., & Serrano, E. (2013). Quantifying tracer transport in the tropical lower stratosphere using WACCM. *Atmospheric Chemistry and Physics*, *13*(21), 10591.

Ackerman, T. P., Liou, K.-N., Valero, F. P., & Pfister, L. (1988). Heating rates in tropical anvils. *Journal of the Atmospheric Sciences*, *45*(10), 1606–1623.

Anderson, J. G., Wilmouth, D. M., Smith, J. B., & Sayres, D. S. (2012). UV dosage levels in summer: Increased risk of ozone loss from convectively injected water vapor. *Science*, *337*(6096), 835–839.

Andrews, D. G., Holton, J. R., & Leovy, C. B. (1987). *Middle atmosphere dynamics* (Vol. 40). Cambridge, MA: Academic press.

Arnone, E., Smith, A., Enell, C.-F., Kero, A., & Dinelli, B. (2014). WACCM climate chemistry sensitivity to sprite perturbations. *Journal of Geophysical Research: Atmospheres*, *119*, 6958–6970. https://doi.org/10.1002/2013JD020825

Bannister, R., O'neill, A., Gregory, A., & Nissen, K. (2004). The role of the south-east Asian monsoon and other seasonal features in creating the "tape-recorder" signal in the unified model. *Quarterly Journal of the Royal Meteorological Society*, *130*(599), 1531–1554.

Bergman, J. W., Fierli, F., Jensen, E. J., Honomichl, S., & Pan, L. L. (2013). Boundary layer sources for the asian anticyclone: Regional contributions to a vertical conduit. *Journal of Geophysical Research: Atmospheres*, *118*, 2560–2575. https://doi.org/10.1002/jgrd.50142

Boehm, M. T., & Lee, S. (2003). The implications of tropical Rossby waves for tropical tropopause cirrus formation and for the equatorial upwelling of the Brewer-Dobson circulation. *Journal of the Atmospheric Sciences*, *60*(2), 247–261.

Bosilovich, M. G. (2015). *MERRA-2: Initial evaluation of the climate*. Greenbelt, MD, USA: National Aeronautics and Space Administration, Goddard Space Flight Center.

Butchart, N., Anstey, J. A., Hamilton, K., Osprey, S., McLandress, C., Bushell, A. C., et al. (2018). Overview of experiment design and comparison of models participating in phase 1 of the SPARC Quasi-Biennial Oscillation initiative (QBOi). *Geoscientific Model Development*, *11*(3), 1009–1032.

Calvo, N., Garcia, R., Randel, W., & Marsh, D. (2010). Dynamical mechanism for the increase in tropical upwelling in the lowermost tropical stratosphere during warm ENSO events. *Journal of the Atmospheric Sciences*, *67*(7), 2331–2340.

Charlton-Perez, A. J., Baldwin, M. P., Birner, T., Black, R. X., Butler, A. H., Calvo, F. N., et al. (2013). On the lack of stratospheric dynamical variability in low-top versions of the CMIP5 models. *Journal of Geophysical Research: Atmospheres*, *118*, 2494–2505. https://doi.org/10.1002/jgrd.50125

Chen, G., & Sun, L. (2011). Mechanisms of the tropical upwelling branch of the Brewer-Dobson circulation: The role of extratropical waves. *Journal of the Atmospheric Sciences*, *68*(12), 2878–2892.

Dee, D. P., Uppala, S. M., Simmons, A. J., Berrisford, P., Poli, P., Kobayashi, S., et al. (2011). The ERA-Interim reanalysis: Configuration and performance of the data assimilation system. *Quarterly Journal of the Royal Meteorological Society*, *137*(656), 553–597.

Dessler, A., & Sherwood, S. (2004). Effect of convection on the summertime extratropical lower stratosphere. *Journal of Geophysical Research*, *109*, D23301. https://doi.org/10.1029/2004JD005209

Dethof, A., O'Neill, A., Slingo, J., & Smit, H. (1999). A mechanism for moistening the lower stratosphere involving the Asian summer monsoon. *Quarterly Journal of the Royal Meteorological Society*, *125*(556), 1079–1106.

Dunkerton, T. J. (1995). Evidence of meridional motion in the summer lower stratosphere adjacent to monsoon regions. *Journal of Geophysical Research*, *100*(D8), 16,675–16,688.

Dvortsov, V. L., & Solomon, S. (2001). Response of the stratospheric temperatures and ozone to past and future increases in stratospheric humidity. *Journal of Geophysical Research*, *106*(D7), 7505–7514.

Eyring, V., Lamarque, J.-F., & Hess, P. (2013). Overview of IGAC/SPARC Chemistry-Climate Model Initiative (CCMI) Community simulations in support of upcoming ozone and climate assessments, Tech. Rep. SPARC Newsletter No. 40, 48–66.

Folkins, I., Oltmans, S. J., & Thompson, A. M. (2000). Tropical convective outflow and near surface equivalent potential temperatures. *Geophysical Research Letters*, *27*(16), 2549–2552.

Forster, P. M. F., & Shine, K. P. (1999). Stratospheric water vapour changes as a possible contributor to observed stratospheric cooling. *Geophysical Research Letters*, *26*(21), 3309–3312.

Fueglistaler, S., Liu, Y. S., Flannaghan, T. J., Haynes, P. H., Dee, D. P., Read, W. J., et al. (2013). The relation between atmospheric humidity and temperature trends for stratospheric water. *Journal of Geophysical Research: Atmospheres*, *118*, 1052–1074. https://doi.org/10.1002/jgrd.50157

Gage, K., McAfee, J., Carter, D., Ecklund, W., Riddle, A., Balsley, B., & REID, G. (1991). Long-term mean vertical motion over the tropical pacific: Wind-profiling Doppler radar measurements. *Science*, *254*(5039), 1771–1773.

Garcia, R. R., & Randel, W. J. (2008). Acceleration of the Brewer-Dobson circulation due to increases in greenhouse gases. *Journal of the Atmospheric Sciences*, *65*(8), 2731–2739.

Garcia, R. R., Smith, A. K., Kinnison, D. E., Cámara, Á. D. L., & Murphy, D. J. (2017). Modification of the gravity wave parameterization in the whole atmosphere community climate model: Motivation and results. *Journal of the Atmospheric Sciences*, *74*(1), 275–291.

Garny, H., Dameris, M., Randel, W., Bodeker, G. E., & Deckert, R. (2011). Dynamically forced increase of tropical upwelling in the lower stratosphere. *Journal of the Atmospheric Sciences*, *68*(6), 1214–1233.

Garny, H., & Randel, W. (2013). Dynamic variability of the Asian monsoon anticyclone observed in potential vorticity and correlations with tracer distributions. *Journal of Geophysical Research: Atmospheres*, *118*, 13,421–13,433. https://doi.org/10.1002/2013JD020908

Garny, H., & Randel, W. J. (2016). Transport pathways from the Asian monsoon anticyclone to the stratosphere. *Atmospheric Chemistry and Physics*, *16*(4), 2703–2718.

Gettelman, A., & Forster, P. M. (2002). A climatology of the tropical tropopause layer. *Journal of the Meteorological Society of Japan Ser. II*, *80*(4B), 911–924.

Gettelman, A., Hegglin, M. I., Son, S.-W., Kim, J., Fujiwara, M., Birner, T., et al. (2010). Multimodel assessment of the upper troposphere and lower stratosphere: Tropics and global trends. *Journal of Geophysical Research*, *115*, D00M08. https://doi.org/10.1029/2009JD013638

Gettelman, A., Kinnison, D. E., Dunkerton, T. J., & Brasseur, G. P. (2004). Impact of monsoon circulations on the upper troposphere and lower stratosphere. *Journal of Geophysical Research*, *109*, D22101. https://doi.org/10.1029/2004JD004878

Gill, A. (1980). Some simple solutions for heat-induced tropical circulation. *Quarterly Journal of the Royal Meteorological Society*, *106*(449), 447–462.

Hardiman, S. C., Boutle, I. A., Bushell, A. C., Butchart, N., Cullen, M. J. P., Field, P. R., et al. (2015). Processes controlling tropical tropopause temperature and stratospheric water vapor in climate models. *Journal of Climate*, *28*(16), 6516–6535.

Haynes, P., McIntyre, M., Shepherd, T., Marks, C., & Shine, K. P. (1991). On the "downward control" of extratropical diabatic circulations by eddy-induced mean zonal forces. *Journal of the Atmospheric Sciences*, *48*(4), 651–678.

Highwood, E., & Hoskins, B. (1998). The tropical tropopause. *Quarterly Journal of the Royal Meteorological Society*, *124*(549), 1579–1604.

Hurrell, J. W., Holland, M. M., Gent, P. R., Ghan, S., Kay, J. E., Kushner, P. J., et al. (2013). The Community Earth System Model: A framework for collaborative research. *Bulletin of the American Meteorological Society*, *94*, 1339–1360. https://doi.org/10.1175/BAMS-D-12-00121.1

Inness, P. M., Slingo, J. M., Woolnough, S. J., Neale, R. B., & Pope, V. (2001). Organization of tropical convection in a GCM with varying vertical resolution: Implications for the simulation of the Madden-Julian Oscillation. *Climate Dynamics*, *17*(10), 777–793.

Jackson, D., Driscoll, S., Highwood, E., Harries, J., & Russell, J. (1998). Troposphere to stratosphere transport at low latitudes as studies using HALOE observations of water vapour 1992–1997. *Quarterly Journal of the Royal Meteorological Society*, *124*(545), 169–192.

Jiang, J. H., Su, H., Zhai, C., Perun, V., Del Genio, A. D., Nazarenko, L. S., et al. (2012). Evaluation of cloud and water vapor simulations in CMIP5 climate models using NASA "A-Train" satellite observations. *Journal of Geophysical Research*, *117*, D14. https://doi.org/10.1029/2011JD017237

Jiang, J. H., Su, H., Zhai, C., Wu, L., Minschwaner, K., Molod, A. M., & Tompkins, A. M. (2015). An assessment of upper troposphere and lower stratosphere water vapor in MERRA, MERRA2, and ECMWF reanalyses using Aura MLS observations. *Journal of Geophysical Research: Atmosphere*, *120*, 11,468–11,485. https://doi.org/10.1002/2015JD023752

Jin, F., & Hoskins, B. J. (1995). The direct response to tropical heating in a baroclinic atmosphere. *Journal of the Atmospheric Sciences*, *52*(3), 307–319.

Kim, J., Grise, K. M., & Son, S.-W. (2013). Thermal characteristics of the cold-point tropopause region in CMIP5 models. *Journal of Geophysical Research: Atmospheres*, *118*, 8827–8841.

Kim, J., Randel, W. J., & Birner, T. (2018). Convectively driven tropopause-level cooling and its influences on stratospheric moisture. *Journal of Geophysical Research: Atmospheres*, *123*, 590–606.

Kuang, Z., & Bretherton, C. S. (2004). Convective influence on the heat balance of the tropical tropopause layer: A cloud-resolving model study. *Journal of the atmospheric sciences*, *61*, 2919–2927.

Kunz, A., Pan, L., Konopka, P., Kinnison, D., & Tilmes, S. (2011). Chemical and dynamical discontinuity at the extratropical tropopause based on START08 and WACCM analyses. *Journal of Geophysical Research*, *116*, D24302. https:doi.org/10.1029/2011JD016686

Lamarque, J.-F., Emmons, L. K., Hess, P. G., Kinnison, D. E., Tilmes, S., Vitt, F., et al. (2012). CAM-chem: Description and evaluation of interactive atmospheric chemistry in the CESM. *Geoscientific Model Development*, *5*(2), 369.

Li, Q., Jacob, D. J., Park, R., Wang, Y. X., Heald, C. L., Hudman, R., et al. (2005). North American pollution outflow and the trapping of convectively lifted pollution by upper-level anticyclone. *Journal of Geophysical Research*, *110*, D10301. https://doi.org/10.1029/2004JD005039

Li, Q., Jiang, J. H., Wu, D. L., Read, W. G., Livesey, N. J., Waters, J. W., et al. (2005). Convective outflow of south Asian pollution: A global CTM simulation compared with EOS MLS observations. *Geophysical Research Letters*, *32*, L14826. https://doi.org/10.1029/2005GL022762

Lindzen, R. S., & Fox-Rabinovitz, M. (1989). Consistent vertical and horizontal resolution. *Monthly Weather Review*, *117*(11), 2575–2583.

Livesey, N. J., Read, W. G., Wagner, P. A., Froidevaux, L., Lambert, A., Manney, G. L., et al. (2018). Earth Observing System (EOS) Aura Microwave Limb Sounder (MLS) version 4.2× level 2 data quality and description document, JPL D-33509 Rev. D. Retrieved from https://mls.jpl.nasa.gov/data/v4-2_data_quality_document.pdf

Marsh, D. R., Mills, M. J., Kinnison, D. E., Lamarque, J.-F., Calvo, N., & Polvani, L. M. (2013). Climate change from 1850 to 2005 simulated in CESM1 (WACCM). *Journal of Climate*, *26*(19), 7372–7391.

Maycock, A. C., Joshi, M. M., Shine, K. P., & Scaife, A. A. (2013). The circulation response to idealized changes in stratospheric water vapor. *Journal of Climate*, *26*(2), 545–561.

Mills, M. J., Richter, J. H., Tilmes, S., Kravitz, B., MacMartin, D. G., Glanville, A. A., et al. (2017). Radiative and chemical response to interactive stratospheric sulfate aerosols in fully coupled CESM1 (WACCM). *Journal of Geophysical Research: Atmospheres*, *122*, 13,061–13,078. http://doi.org/10.1002/2017JD027006

Mills, M. J., Schmidt, A., Easter, R., Solomon, S., Kinnison, D. E., Ghan, S. J., et al. (2016). Global volcanic aerosol properties derived from emissions, 1990–2014, using CESM1 (WACCM). *Journal of Geophysical Research: Atmospheres*, *121*, 2332–2348. http://doi.org/10.1002/2015JD024290

Milz, M., von Clarmann, T., Fischer, H., Glatthor, N., Grabowski, U., HöPfner, M., et al. (2005). Water vapor distributions measured with the Michelson interferometer for passive atmospheric sounding on board Envisat (MIPAS/Envisat). *Journal of Geophysical Research*, *110*, D24307. https://doi.org/10.1029/2005JD005973

Morgenstern, O., Hegglin, M., Rozanov, E., O'Connor, F., Luke Abraham, N., Akiyoshi, H., & Archibald, A. T. (2017). Review of the global models used within phase 1 of the Chemistry-Climate Model Initiative (CCMI). *Geoscientific Model Development*, *10*(2), 639–671.

Neale, R. B., Ritcher, J. H., Conley, A. J., Park, S., Lauritzen, P. H., Gettelman, A., & Williamson, D. L. (2010). Description of the NCAR Community Atmosphere Model (*CAM 5.0*). Boulder, CO: NCAR Tech. Note NCAR/TN-486+ STR.

Norton, W. (2001). Longwave heating of the tropical lower stratosphere. *Geophysical Research Letters*, *28*(19), 3653–3656.

Norton, W. (2006). Tropical wave driving of the annual cycle in tropical tropopause temperatures. Part II: Model results. *Journal of the atmospheric sciences*, *63*(5), 1420–1431.

Oleson, K., Lawrence, D. M., Bonan, G. B., Flanner, M. G., Kluzek, E., Lawrence, P. J., et al. (2013). Technical description of version 4.5 of the Community Land Model (CLM).

Pan, L. L., Honomichl, S. B., Kinnison, D. E., Abalos, M., Randel, W. J., Bergman, J. W., & Bian, J. (2016). Transport of chemical tracers from the boundary layer to stratosphere associated with the dynamics of the Asian summer monsoon. *Journal of Geophysical Research: Atmospheres*, *121*, 14,159–14,174. https://doi.org/10.1002/2016JD025616

Park, M., Randel, W. J., Emmons, L. K., Bernath, P. F., Walker, K. A., & Boone, C. D. (2008). Chemical isolation in the Asian monsoon anticyclone observed in Atmospheric Chemistry Experiment (ACE-FTS) data. *Atmospheric Chemistry and Physics*, *8*(3), 757–764.

Park, M., Randel, W. J., Emmons, L. K., & Livesey, N. J. (2009). Transport pathways of carbon monoxide in the Asian summer monsoon diagnosed from model of ozone and related tracers (MOZART). *Journal of Geophysical Research*, *114*, D08303.

Park, M., Randel, W. J., Gettelman, A., Massie, S. T., & Jiang, J. H. (2007). Transport above the Asian summer monsoon anticyclone inferred from aura microwave limb sounder tracers. *Journal of Geophysical Research*, *112*, D16309. https://doi.org/10.1029/2006JD008294

Park, M., Randel, W. J., Kinnison, D. E., Garcia, R. R., & Choi, W. (2004). Seasonal variation of methane, water vapor, and nitrogen oxides near the tropopause: Satellite observations and model simulations. *Journal of Geophysical Research*, *109*, D03302. https://doi.org/10.1029/2003JD003706

Ploeger, F., Gottschling, C., Griessbach, S., Grooß, J. U., Guenther, G., Konopka, P., et al. (2015). A potential vorticity-based determination of the transport barrier in the Asian summer monsoon anticyclone. *Atmospheric Chemistry and Physics*, *15*(22), 13,145–13,159.

Ploeger, F., Günther, G., Konopa, P., Fueglistaler, S., Müller, R., Hoppe, C., et al. (2013). Horizontal water vapor transport in the lower stratosphere from subtropics to high latitudes during boreal summer. *Journal of Geophysical Research: Atmospheres*, *118*, 8111–8127. https://doi.org/10.1002/jgrd.50636

Ploeger, F., Konopka, P., Walker, K., & Riese, M. (2017). Quantifying pollution transport from the Asian monsoon anticyclone into the lower stratosphere. *Atmospheric Chemistry and Physics*, *17*(11), 7055–7066.

Plumb, R. A., & Eluszkiewicz, J. (1999). The Brewer-Dobson circulation: Dynamics of the tropical upwelling. *Journal of the atmospheric sciences*, *56*(6), 868–890.

Pope, V., Pamment, J., Jackson, D., & Slingo, A. (2001). The representation of water vapor and its dependence on vertical resolution in the Hadley Centre climate model. *Journal of Climate*, *14*(14), 3065–3085.

Popovic, J. M., & Plumb, R. A. (2001). Eddy shedding from the upper-tropospheric Asian monsoon anticyclone. *Journal of the Atmospheric Sciences*, *58*(1), 93–104.

Qu, X., & Huang, G. (2015). The decadal variability of the tropical indian ocean SST—The south Asian high relation: CMIP5 model study. *Climate Dynamics*, *45*(1-2), 273–289.

Randel, W. J., & Jensen, E. J. (2013). Physical processes in the tropical tropopause layer and their roles in a changing climate. *Nature Geoscience*, *6*(3), 169–176.

Randel, W. J., & Park, M. (2006). Deep convective influence on the Asian summer monsoon anticyclone and associated tracer variability observed with Atmospheric Infrared Sounder (AIRS). *Journal of Geophysical Research*, *111*, D12314. https://doi.org/10.1029/2005JD006490

Randel, W. J., & Wu, F. (2005). Kelvin wave variability near the equatorial tropopause observed in GPS radio occultation measurements. *Journal of Geophysical Research*, *110*, D03102. https://doi.org/10.1029/2004JD005006

Randel, W. J., Wu, F., Gettelman, A., Russell, J., Zawodny, J. M., & Oltmans, S. J. (2001). Seasonal variation of water vapor in the lower stratosphere observed in halogen occultation experiment data. *Journal of Geophysical Research*, *106*(D13), 14,313–14,325.

Randel, W. J., Zhang, K., & Fu, R. (2015). What controls stratospheric water vapor in the NH summer monsoon regions? *Journal of Geophysical Research: Atmospheres*, *120*, 7988–8001. https://doi.org/10.1002/2015JD023622

Reid, G., & Gage, K. (1996). The tropical tropopause over the western pacific: Wave driving, convection, and the annual cycle. *Journal of Geophysical Research*, *101*(D16), 21,233–21,241.

Richter, J. H., Sassi, F., & Garcia, R. R. (2010). Toward a physically based gravity wave source parameterization in a general circulation model. *Journal of the Atmospheric Sciences*, *67*(1), 136–156.

Richter, J. H., Solomon, A., & Bacmeister, J. T. (2014). Effects of vertical resolution and nonorographic gravity wave drag on the simulated climate in the Community Atmosphere Model, version 5. *Journal of Advances in Modeling Earth Systems*, *6*, 357–383.

Rienecker, M. M., Suarez, M. J., Gelaro, R., Todling, R., Bacmeister, J., Liu, E., et al. (2011). MERRA: NASA's Modern-Era Retrospective analysis for Research and Applications. *Journal of Climate*, *24*(14), 3624–3648.

Rodwell, M. J., & Hoskins, B. J. (1996). Monsoons and the dynamics of deserts. *Quarterly Journal of the Royal Meteorological Society*, *122*(534), 1385–1404.

Roeckner, E., Brokopf, R., Esch, M., Giorgetta, M., Hagemann, S., Kornblueh, L., et al. (2006). Sensitivity of simulated climate to horizontal and vertical resolution in the ECHAM5 atmosphere model. *Journal of Climate*, *19*(16), 3771–3791.

Rosenlof, K. H., Tuck, A. F., Kelly, K. K., Russell, J. M., & McCormick, M. P. (1997). Hemispheric asymmetries in water vapor and inferences about transport in the lower stratosphere. *Journal of Geophysical Research*, *102*(D11), 13,213–13,234.

Ryu, J.-H., & Lee, S. (2010). Effect of tropical waves on the tropical tropopause transition layer upwelling. *Journal of the Atmospheric Sciences*, *67*(10), 3130–3148.

Schoeberl, M., & Dessler, A. (2011). Dehydration of the stratosphere. *Atmospheric Chemistry and Physics*, *11*(16), 8433–8446.

Schwartz, M. J., Read, W. G., Santee, M. L., Livesey, N. J., Froidevaux, L., Lambert, A., & Manney, G. L. (2013). Convectively injected water vapor in the North American summer lowermost stratosphere. *Geophysical Research Letters*, *40*, 2316–2321. https://doi.org/10.1002/grl.50421

Sherwood, S. C., Horinouchi, T., & Zeleznik, H. A. (2003). Convective impact on temperatures observed near the tropical tropopause. *Journal of the Atmospheric Sciences*, *60*(15), 1847–1856.

Smith, K. L., Neely, R., Marsh, D., & Polvani, L. M. (2014). The Specified Chemistry Whole Atmosphere Community Climate Model (SC-WACCM). *Journal of Advances in Modeling Earth Systems*, *6*, 883–901.

Solomon, S., Kinnison, D., Garcia, R. R., Bandoro, J., Mills, M., Wilka, C., et al. (2016). Monsoon circulations and tropical heterogeneous chlorine chemistry in the stratosphere. *Geophysical Research Letters*, *43*, 12,624–12,633. https://doi.org/10.1002/2016GL071778

Solomon, S., Rosenlof, K. H., Portmann, R. W., Daniel, J. S., Davis, S. M., Sanford, T. J., & Plattner, G.-K. (2010). Contributions of stratospheric water vapor to decadal changes in the rate of global warming. *Science*, *327*(5970), 1219–1223.

Taguchi, M. (2009). Wave driving in the tropical lower stratosphere as simulated by WACCM. Part I: Annual cycle. *Journal of the Atmospheric Sciences*, *66*(7), 2029–2043.

Takahashi, H., Su, H., & Jiang, J. H. (2016). Error analysis of upper tropospheric water vapor in CMIP5 models using "A-Train" satellite observations and reanalysis data. *Climate dynamics*, *46*(9-10), 2787–2803.

Taylor, K. E., Stouffer, R. J., & Meehl, G. A. (2012). An overview of CMIP5 and the experiment design. *Bulletin of the American Meteorological Society*, *93*(4), 485–498.

Tian, B., Fetzer, E. J., Kahn, B. H., Teixeira, J., Manning, E., & Hearty, T. (2013). Evaluating CMIP5 models using airs tropospheric air temperature and specific humidity climatology. *Journal of Geophysical Research: Atmospheres*, *118*, 114–134. https://doi.org/10.1029/2012JD018607

Tilmes, S., Lamarque, J. F., Emmons, L. K., Kinnison, D. E., Marsh, D., Garcia, R. R., et al. (2016). Representation of the Community Earth System Model (CESM1) CAM4-chem within the Chemistry-Climate Model Initiative (CCMI). *Geoscientific Model Development*, *9*(5), 1853–1890. https://doi.org/10.5194/gmd-9-1853-2016

Tsuda, T., Murayama, Y., Wiryosumarto, H., Harijono, S. W. B., & Kato, S. (1994). Radiosonde observations of equatorial atmosphere dynamics over Indonesia: 1. Equatorial waves and diurnal tides. *Journal of Geophysical Research*, *99*(D5), 10,491–10,505.

Uma, K., Das, S. K., & Das, S. S. (2014). A climatological perspective of water vapor at the UTLS region over different global monsoon regions: Observations inferred from the Aura-MLS and reanalysis data. *Climate Dynamics*, *43*(1-2), 407–420.

Wang, W., Matthes, K., Schmidt, T., & Neef, L. (2013). Recent variability of the tropical tropopause inversion layer. *Geophysical Research Letters*, *40*, 6308–6313. https://doi.org/10.1002/2013GL058350

Wright, J., Fu, R., Fueglistaler, S., Liu, Y., & Zhang, Y. (2011). The influence of summertime convection over southeast Asia on water vapor in the tropical stratosphere. *Journal of Geophysical Research*, *116*, D12302. https://doi.org/10.1029/2010JD015416

Wu, Y., & Shaw, T. A. (2016). The impact of the Asian summer monsoon circulation on the tropopause. *Journal of Climate*, *29*(24), 8689–8701.

Zhang, K., Fu, R., Wang, T., & Liu, Y. (2016). Impact of geographic variations of the convective and dehydration center on stratospheric water vapor over the Asian monsoon region. *Atmospheric Chemistry and Physics*, *16*(12), 7825–7835.

Zhou, X., & Holton, J. R. (2002). Intraseasonal variations of tropical cold-point tropopause temperatures. *Journal of Climate*, *15*(12), 1460–1473.